Received 28 March 2022; revised 2 May 2022; accepted 24 May 2022.
Date of publication 30 May 2022; date of current version 9 June 2022.

Digital Object Identifier 10.1109/OJUFFC.2022.3178972

An Improved Lumped Element Model for Circular-Shape pMUTs

SEDAT PALA AND LIWEI LIN (Member, IEEE)

Berkeley Sensor and Actuator Center, Berkeley, CA 94720 USA
Department of Mechanical Engineering, University of California at Berkeley, Berkeley, CA 94720 USA
CORRESPONDING AUTHOR: S. PALA (spala@berkeley.edu)

ABSTRACT This paper presents an improved lumped element model for clamped, circular-shape, piezoelectric micromachined ultrasonic transducers (pMUTs). A small signal equivalent circuit is developed to include electrical, mechanical, and acoustic domains, which are analyzed separately and combined with the associated couplings. For the first time, a two-term mode shape approach is adapted to reveal intrinsic and extrinsic properties of a pMUT, such as equivalent circuit parameters, input impedance, velocity, displacement, bandwidth, quality factor, directivity, and the on-axis pressure in the near and far field. These properties are compared with prior reports in the literature and exact solutions, as well as Finite Element Method (FEM) simulations. The errors relative to exact solution for all these properties are below 0.5%. These improvements in error are from 5x to about 3 orders of magnitude better than those of prior works. As such, the improved model could be helpful in design and simulation tools for pMUTs.

INDEX TERMS Piezoelectric micromachined ultrasonic transducers, pMUT, lumped element model, equivalent circuit model, analytical model, mode shape.

I. INTRODUCTION

MICROMACHINING technologies have unveiled exciting applications for ultrasonic transducers for the last couple of decades. Micromachined ultrasonic transducers (MUTs) are best known for their capability to provide medical diagnostics in the form of ultrasonic images [1] in human body or liquid [2]. In recent years, MUT applications have been expanded in the air medium such as range finders [3]–[5], fingerprint sensing [6], [7], human machine interface [8], [9], gesture recognition [10], surface metrology [11], [12], and more. There are two transduction mechanisms in MUTs: the capacitive [13] and piezoelectric scheme [14]. Performance enhancement studies can be summarized in two approaches; (1) optimal geometric designs such as collapse mode [15] in capacitive MUTs (cMUTs) or curved [16], ring [17], free [18] and pinned [19] boundary, bimorph [20] structures in piezoelectric MUTs (pMUTs); and (2) thin film materials with high piezoelectric properties such as PZT [21] and AlN [22]. In this study, pMUTs are investigated since they have shown prominent features in air applications such as no need for a bias voltage and the large displacement under the flexural vibration mode.

In parallel to the performance enhancement efforts, an accurate analytical model is needed to gain a better understanding of the physical mechanism for improved structures. As stated in [23], the purpose of computation is to have insights and not just pure numbers. Although constructing a better model takes time, once it is done it can be used forever [24]. Hence, there has been great effort to construct improved models focusing on transduction mechanisms [25], mechanical structures [16], and complete physics analysis [26]. However, these models are mostly complicated with advanced functions which result in unpractical equivalent circuit models.

In this paper, we present an improved lumped element model for clamped circular-shape pMUTs. It starts with the mechanical structure to reflect important intrinsic and extrinsic design parameters. Then, a two-term mode shape approach is used in three domains: mechanical, electrical, and acoustic. An approximate energy-based method, Rayleigh-Ritz, is utilized to predict more accurate mode shapes and the Lumped elements and equivalent circuit model are presented with comparisons of literature and exact solution. An improved small signal electro-mechano-acoustic equivalent model is established to analyze several key parameters such as: electrical input impedance, frequency response, bandwidth, quality factor, directivity, and the acoustic on-axis pressure in the near and far fields. The model has been

verified with FEM simulations to calculate the errors in all design parameters as less than 0.5% in terms of accuracy compared to prior literature work. These results indicate that this energy-based method can be utilized to obtain accurate mode shapes as well as design parameters for circular-shape pMUTs. Furthermore, the methodology should also be applicable for other pMUT structures such as rectangle, ring shapes and the dual electrode bimorph designs.

II. IMPROVED LUMPED ELEMENT MODEL FOR A pMUT CELL

The physical analysis of a unimorph, clamped, circular pMUT shown in Fig. 1.a is separated into three domains: mechanical, electrical, and acoustic. In the mechanical domain, a two-term mode shape approach based on the approximate energy method is used. In the electrical domain, the strain field effect is analyzed in order to obtain an optimum electrode coverage area and the effects of the deformed shape on the acoustic radiation impedance are investigated in the acoustic domain. Finally, all domains are integrated using an equivalent circuit model with important parameters such as the electrical capacitance, electromechanical transduction ratio, mechanical impedance, and acoustic impedance.

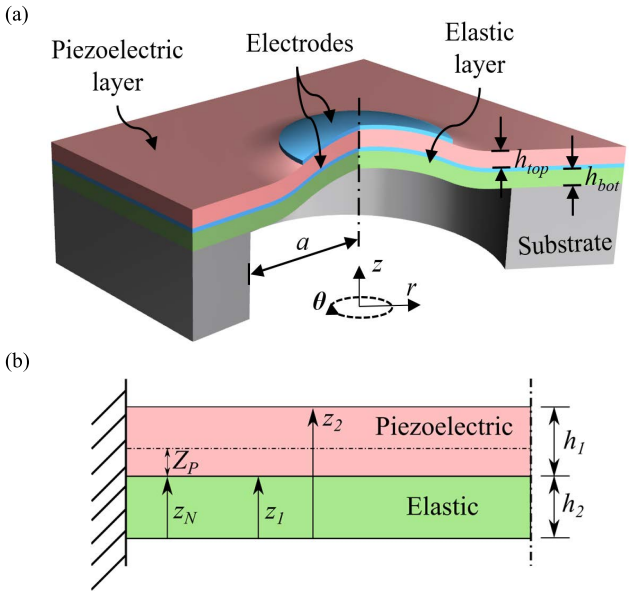

FIGURE 1. (a) 3-D schematics of a clamped circular-shape unimorph pMUT with deformed diaphragm showing the layers and electrodes. (b) Cross sectional view of the vibrating diaphragm with geometric parameters in the thickness direction.

A. pMUT STRUCTURE AND DESIGN CONSIDERATIONS

In this study, a circular-shape diaphragm free to vibrate in the transverse direction and clamped at the outer edge (see Fig. 1.a) is analyzed. The circular geometry is mostly preferred due to the mechano-acoustic transduction. For the same surface area, thickness, applied force, and boundary conditions, the mean displacement of the fundamental mode over the surface area is the largest in the circular diaphragm as compared to those in the triangular, rectangular, pentagon, etc. diaphragms. This circular diaphragm composes of multiple layers for the pMUT: elastic, piezoelectric and electrodes, as shown in Fig. 1b.

There are many characteristic parameters in the pMUT design to optimize the performance. First and most importantly, the acoustical power output is the key element to improve both the working distance and signal to noise ratio (SNR). A maximum acoustic pressure is obtained when the diaphragm surface velocity is maximized. In general, the displacement at the resonance is equal to the low frequency or quasistatic displacement multiplied by the quality factor, Q. If only a maximum displacement is considered, a high quality factor is favored. However, the acoustic power output also depends on the radiation impedance which has two components: resistive and reactive part, where power flows through the resistive component; while reactive component stores the power. As such, an ultrasonic device is favored to have the high resistive and low reactive component to produce large outputs, or a low quality factor. Higher resistive component decreases the quality factor counteracting the high displacement requirement. As such, there is a balance between the acoustic power and surface displacement during the design process. Another design consideration is the bandwidth which affects the mechano-acoustic transduction efficiency and axial resolution. A device with high bandwidth will result in a high loss mechanism in the mechanical structure. While most loss mechanisms are unwanted energy dissipations, the loss due to the acoustic radiation is encouraged to produce large power flow from the mechanical domain to the acoustic domain in the ambient environment, which is called the mechano-acoustic transduction efficiency. To maximize this efficiency under a large bandwidth, the characteristic mechanical impedance of the transducer should be matched to that of the medium and this bandwidth consideration has a strong correlation with the quality factor. As stated before, a high quality factor is desired for higher displacement amplitude at the resonance and a high bandwidth is desired for the high power output flow. However, since the bandwidth is generally inversely proportional to quality factor such that a design balance must be reached. Finally, the electromechanical coupling coefficient is defined as a change in the stiffness or capacitance as response to the change in the electrical or mechanical boundary conditions. The electromechanical coupling coefficient can also be defined as a portion of the total input electrical energy stored in the mechanical form for a static voltage [27]. It is highly dependent on the piezoelectric coefficient and the geometric property, such as the stress-strain distribution inside the diaphragm. All combined, these domains and coupling between them are analyzed separately in the following sections. An energy based, intuitive method is followed in order to obtain lumped parameters accurately in the equivalent circuit analysis.

B. MECHANICAL DOMAIN

In the mechanical domain, the transverse vibration of a circular disk clamped at the outer edge is analyzed. Although the exact solution of a transversely vibrating circular disk is available in the literature [27]–[32], a more compact and easy-to-handle approximate solution is preferred. The exact solution is also given here for the sake of completeness and comparison. The equation of motion is first derived with an assumption that the thin plate theory applies to work in the two dimensions instead of three dimensions [31]–[34]. The displacement of each point on the plate is described by only the displacement of mid-plane (neutral plane). The most general form of equation of motion of a transversely vibrating thin plate without any dissipative elements is given as [33]:

$$D\nabla^4 w(r,\theta,t) + \Lambda \frac{\partial^2 w(r,\theta,t)}{\partial t^2} = f(r,\theta,t) \tag{1}$$

where $w(r, \theta, t)$ is the transverse displacement; $f(r, \theta, t)$ is transversely applied external force; Λ is the surface density; and D is the flexural rigidity. For a multilayer structure as shown in Fig. 1b, Λ and D are given by [33]:

$$\Lambda = \sum_{i=1}^{q} \rho_i h_i$$
$$D = \sum_{i=1}^{q} \frac{Y_i}{3\left(1-v_i^2\right)} \left[(z_i - z_N)^3 - (z_{i-1} - z_N)^3\right] \tag{2}$$

where q is the number of layers; ρ is the layer density; h is the layer thickness; Y is the Young's modulus of the layer; v is Poisson's ratio of the layer; z_N is the distance of the neutral axis from the bottom; and z_i is the distance measured from the bottom of the whole stacked layer to the top surface of each layer. For the same structure, the neutral axis is calculated [21]:

$$z_N = \frac{1}{2} \frac{\sum_{i=1}^{q} \frac{Y_i\left(z_i^2 - z_{i-1}^2\right)}{1-v_i^2}}{\sum_{i=1}^{q} \frac{Y_i(z_i - z_{i-1})}{1-v_i^2}} \tag{3}$$

where z_i is given as:

$$z_i = \sum_{j=0}^{i} h_j \tag{4}$$

The exact solution to the axisymmetric modes of the undamped, free vibration of clamped diaphragm can be obtained after applying the separation of variables technique two times; one for the separation of time terms and one for the separation of spatial coordinates [31].

$$W_{0n}(r) = J_0(k_{0n}r) - \frac{J_0(k_{0n}a)}{I_0(k_{0n}a)} I_0(k_{0n}r) \tag{5}$$

where a is the radius of the diaphragm; r is the radial coordinate given in Fig. 1a; J_n and I_n are the Bessel's function and modified Bessel's function, respectively; and k_{0n} is the mode shape dependent parameter. The mode-of-interest is the one which has the largest volumetric mean velocity. In general, ultrasonic transducers are excited at the fundamental mode (where n is equal to zero) which is axisymmetric about the center line of the diaphragm. The mode shape dependent parameter becomes k_{00} and the multiplication with the radius a is equal to 3.196 [33]. The exact fundamental mode shape and the corresponding natural frequency are given by [26]:

$$W_{00}(r) = J_0(k_{00}r) - \frac{J_0(k_{00}a)}{I_0(k_{00}a)} I_0(k_{00}r)$$
$$\omega_{00} = k_{00}^2 \sqrt{\frac{D}{\Lambda}} \tag{6}$$

From the designer perspective, the exact solution given above is difficult to handle since it contains advanced functions like Bessel's functions. In order to have more intuitive and accessible design procedure, an approximate solution with better accuracy than the one used in the literature is developed.

The Rayleigh-Ritz method is an energy based, approximate method for vibration problems, which usually gives sufficiently enough accurate solutions for the small number of lowest modes. This method is suitable for acoustic applications, since ultrasonic transducers are excited at the fundamental mode. Here, the vibration frequency of a conservative system (no dissipating elements and non-conservative forces) has a stationary value in the neighborhood of a natural mode which is, in fact, a minimum value in the neighborhood of the fundamental natural mode [35]. In other words, energy is conserved in the system having no dissipative elements, i.e.,

$$V_{\max} = T_{\max} \tag{7}$$

where $V_{\max}$ and $T_{\max}$ are the maximum potential and kinetic energies, respectively. The kinetic energy is a function of the square of the velocity, which can be separated in spatial and time dependent terms as:

$$T_{\max} = \omega^2 {T_{\max}}^* \tag{8}$$

where ${T_{\max}}^*$ is the maximum kinetic energy solely dependent on spatial coordinates, and ω is the frequency of vibration. Rayleigh's quotient is defined as the ratio of the maximum potential and kinetic energies and given by [29]:

$$R = \omega^2 = \frac{V_{\max}}{{T_{\max}}^*} \tag{9}$$

The shape of the deformation is approximated by trial functions, $\phi(r)$. The fundamental assumed mode shape, $W_0(r)$, is constructed by the superposition of trial functions as:

$$W_0(r) = \sum_{i=1}^{p} c_i \phi_i(r) \tag{10}$$

where p is the number of trial functions used. Trial functions are selected among the admissible set satisfying the geometric boundary conditions, which are resulted from pure geometric compatibility like displacement and slope.

It is possible to calculate several natural frequencies and corresponding mode shapes at once. As p increases, the accuracy of the mode shapes and natural frequencies increases

TABLE 1. Comparison of natural Frequency and mode shape calculations for the fundamental mode of a clamped circular plate.

Solution	Natural Frequency, ω_0 ,[rad/s]	Mode Shape, $W_0(r/a)$
Exact [26]	$\frac{10.21}{a^2}\sqrt{\frac{D}{\Lambda}}$	$J_0\left(3.196\left(\frac{r}{a}\right)\right)-\frac{J_0(3.196)}{I_0(3.196)}I_0\left(3.196\left(\frac{r}{a}\right)\right)$
Literature [37]	$\frac{10.33}{a^2}\sqrt{\frac{D}{\Lambda}}$	$\left[1-\left(\frac{r}{a}\right)^2\right]^2$
This Work	$\frac{10.22}{a^2}\sqrt{\frac{D}{\Lambda}}$	$0.754\left[1-\left(\frac{r}{a}\right)^2\right]^2+0.246\left[1-\left(\frac{r}{a}\right)^2\right]^3$

* The parameters in the equations are explained in the text.

and the most significant improvement is on the first natural frequency. Effect of the improvement decreases from the first to the last mode shape of interest. The calculated natural frequency always approaches to the real value from top [36] due to additional constraints such as higher stiffness, imposed by the incorrect assumption of modes, which is another indication of that Rayleigh's principle is a minimization method. Using the assumed mode shape, the potential and kinetic energy terms are obtained as [29], [31], [33]:

$$V_{\max} = \frac{D}{2}\int_0^{2\pi}\int_0^{a}\left(\frac{d^2W_0(r)}{dr^2}+\frac{1}{r}\frac{dW_0(r)}{dr}\right)^2 rdrd\theta$$
$$V_{\max} = \frac{1}{2}\vec{c}^{\mathrm{T}}[K]\vec{c}$$
$$T_{\max}{}^* = \frac{\Lambda}{2}\int_0^{2\pi}\int_0^{a}(W_0(r))^2 rdrd\theta$$
$$T_{\max}{}^* = \frac{1}{2}\vec{c}^{\mathrm{T}}[M]\vec{c} \tag{11}$$

where the Ritz coefficient vector is $\vec{c} = [c_1, c_2, ..., c_p]^T$ and $[K]$ and $[M]$ are stiffness and mass matrices, respectively. With these energy terms, Rayleigh's quotient becomes the function of constant coefficients:

$$R(c_1, c_2, \cdots, c_p) = \frac{V_{\max}(c_1, c_2, \cdots, c_p)}{T_{\max}(c_1, c_2, \cdots, c_p)} \tag{12}$$

As stated before, vibration frequencies have stationary value in the neighborhood of natural frequencies. That is the minimum value of Rayleigh' s quotient and it can be found by equating the rate of change of R with respect to the Ritz coefficients (c_i's) to zero.

$$\frac{\partial R}{\partial c_i} = 0, \quad i = 1, 2, \cdots, p$$
$$\frac{\partial R}{\partial \vec{c}} = \frac{1}{T^*{}_{\max}}\left(\frac{\partial V_{\max}}{\partial \vec{c}} - \lambda\frac{\partial T^*{}_{\max}}{\partial \vec{c}}\right) = \vec{0} \tag{13}$$

where λ is the eigenvalue of the eigenvalue problem constructed by the mass and stiffness matrices $[M]$ and $[K]$ obtained by the partial derivation of the maximum potential and kinetic energies with respect to Ritz coefficients [33]:

$$\frac{\partial V_{\max}}{\partial \vec{c}} = \vec{c}^{\mathrm{T}}[K]$$
$$\frac{\partial T^*_{\max}}{\partial \vec{c}} = \vec{c}^{\mathrm{T}}[M] \tag{14}$$

Then the eigenvalue problem of order p is defined as follows:

$$[[K] - \lambda[M]]\vec{c} = \vec{0} \tag{15}$$

Eigenvalues are the Rayleigh quotients for each mode and corresponding eigenvectors are the Ritz coefficient vectors. The two boundary conditions for the clamped disk are the geometric boundary conditions and they are given as zero displacement and zero slope at the clamped edge. Therefore, the trial functions are selected among the set given by:

$$\phi_i(r) = \left[1-\left(\frac{r}{a}\right)^2\right]^{i+1}, \quad i = 1, 2 \tag{16}$$

Then the assumed mode shape is (p=*2*):

$$W^0(r) = c_1\left[1-\left(\frac{r}{a}\right)^2\right]^2 + c_2\left[1-\left(\frac{r}{a}\right)^2\right]^3 \tag{17}$$

where c_1 and c_2 are Ritz coefficients to be determined in the minimization of Rayleigh's quotient as explained. The obtained eigenvalue and corresponding eigenvector for the fundamental mode (superscript *0* corresponds to the fundamental mode) are:

$$\lambda^{(0)} = 104.3877 \quad \text{and } c^{(0)} = \begin{bmatrix} 3.067 \\ 1 \end{bmatrix} \tag{18}$$

Table 1 compares the natural frequency and normalized mode shape calculations for the fundamental mode obtained from the exact solution, the literature, and this work. In the natural frequency calculations, error made in literature with respect to the exact solution is 1.14%: however, this error is dropped to 0.03% in this work. While both results are good enough for engineering purposes, this work provides better approximations.

Normalized mode shapes obtained from the exact solution, literature and this work are given in Fig. 2a for comparison.

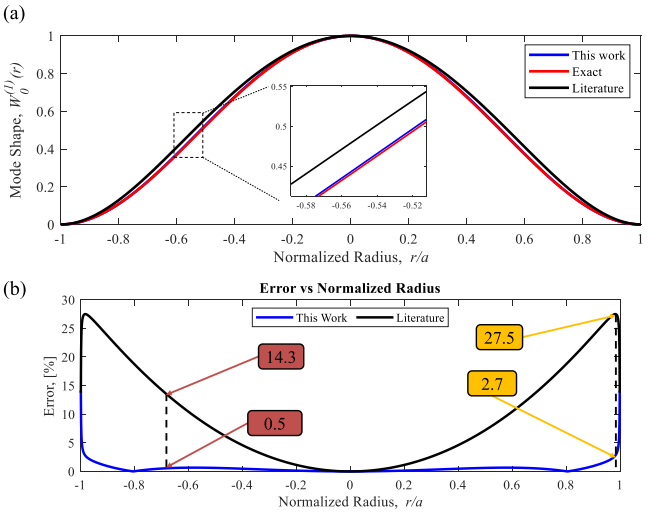

FIGURE 2. Fundamental mode shape and errors made in approximate calculations versus normalized diaphragm radius. (a) The normalized mode shapes for fundamental mode obtained from the exact solution, literature, and this work. (b) Comparison of errors in the mode shape calculation for both the literature and this work with respect to the exact solution. The maximum error percentage at the inner (red color) and outer (orange color) electrode regions are indicated.

Errors made in the literature and this work with respect to the exact solution are given in Fig. 2b. Although inner electrodes are generally used for the pMUT cell, the maximum errors are indicated for both inner and outer electrode regions. The errors in this work are decreased more than one order of magnitude as compared to those of the literature.

C. ELECTRICAL DOMAIN

In the electrical domain, electrical and coupling energy between electrical and mechanical domains are analyzed. The electrical enthalpy approach is utilized rather than just a potential energy for a broader perspective. For a mechanical system only, the Lagrangian approach is enough; however, electrical enthalpy describes piezoelectric as well. For a linear, adiabatic piezoelectric continuum, the electrical enthalpy density is defined as [38]–[40]:

$$\tilde{h}(S,E) = \frac{1}{2}S^T c^E S - S^T eE - \frac{1}{2}E^T \varepsilon^S E \tag{19}$$

where superscript T stands for transpose; superscript E stands for the constant electric field; superscript S stands for the constant strain field; c is the stiffness; S is strain field vector; e is the piezoelectric strain coefficient matrix; E is electric field vector; and ε is dielectric permittivity matrix.

Application specific assumptions based on mechanical and electrical considerations are made to simplify the complicated electrical enthalpy and piezoelectric constitutive equations. From the classical plate theory, shear strains are assumed to be negligible. Hence, the strain field vector has only three normal components. Another assumption is that electrical field applied only in the transverse direction, that is $E = [0\ \ 0\ \ E_3]^T$. Moreover, the material is assumed to be transversely anisotropic, since most of the piezoelectric materials has an in-plane isotropy. Then the three terms in the given electrical enthalpy are reduced to [27], [38], [40]:

$$\begin{aligned}
\tilde{h}_1 &= \frac{1}{2}\left[\frac{Y}{1-\nu^2}\left(S_{rr}^2 + 2\nu S_{rr}S_{\theta\theta} + S_{\theta\theta}^2\right) + \frac{e_{31}^2}{c_{33}^E}E_3^2\right] \\
\tilde{h}_2 &= -\left(S_{rr} + S_{\theta\theta}\right)\left(e_{13} - e_{33}\frac{c_{13}^E}{c_{33}^E}\right)E_3 - \frac{e_{31}^2}{c_{33}^E}E_3^2 \\
\tilde{h}_3 &= -\frac{1}{2}\varepsilon_{33}^S E_3^2
\end{aligned} \tag{20}$$

where all specific enthalpy terms contain the electrical field. In addition, piezoelectric coefficient in thin films is defined by effective coupling coefficient, which is given as [14]:

$$e_{31,f} = e_{31} - e_{33}\frac{c_{13}^E}{c_{33}^E} \tag{21}$$

Rewriting these equations can illustrate the two domains and coupling between these domains.

$$\begin{aligned}
\tilde{h}_{Elastic} &= \frac{1}{2}\frac{Y}{1-\nu^2}\left(S_{rr}^2 + 2\nu S_{rr}S_{\theta\theta} + S_{\theta\theta}^2\right) \\
\tilde{h}_{Coupling} &= -e_{31,f}\left(S_{rr} + S_{\theta\theta}\right)E_3 \\
\tilde{h}_{Electrical} &= -\frac{1}{2}\left(\varepsilon_{33}^S + \frac{e_{31}^2}{c_{33}^E}\right)E_3^2
\end{aligned} \tag{22}$$

where the first term is identical to potential energy given in equation (11) after inserting the strain-displacement relations [41] and taking the integral over the volume. The second term contains both the strain and electrical field, that is the coupling between them through piezoelectric transduction, $e_{31,f}$. The last term is purely electrical and defines the electrical energy.

Electrode design is determined by maximizing the coupling energy term. As seen, the coupling energy term composes of the piezoelectric coefficient, $e_{31,f}$, sum of the strains, I_p, and applied electrical field, V_e. Inserting the strain-displacement relations can yield:

$$H_{Coupling} = -e_{31,f}V_e Z_p I_P \tag{23}$$

where Z_p and I_p are defined as:

$$\begin{aligned}
Z_p &= \frac{1}{h_p}\int_{z_p-h_p-z_N}^{z_p-z_N} z\,dz \\
I_p &= -\int_{A_e}\left(\frac{\partial^2 w}{\partial r^2} + \frac{1}{r}\frac{\partial w}{\partial r}\right)dA_e
\end{aligned} \tag{24}$$

where A_e is electrode area; z_p is the distance from the bottom surface of the layer stack to the top surface of the piezoelectric layer; z_N is the distance from bottom of the layer stack to the neutral axis; and h_p is the thickness of the piezoelectric layer. It is noted that Z_p defines the distance from neutral axis of whole layer stack to midplane of the piezoelectric layer, in other words, it is the moment arm.

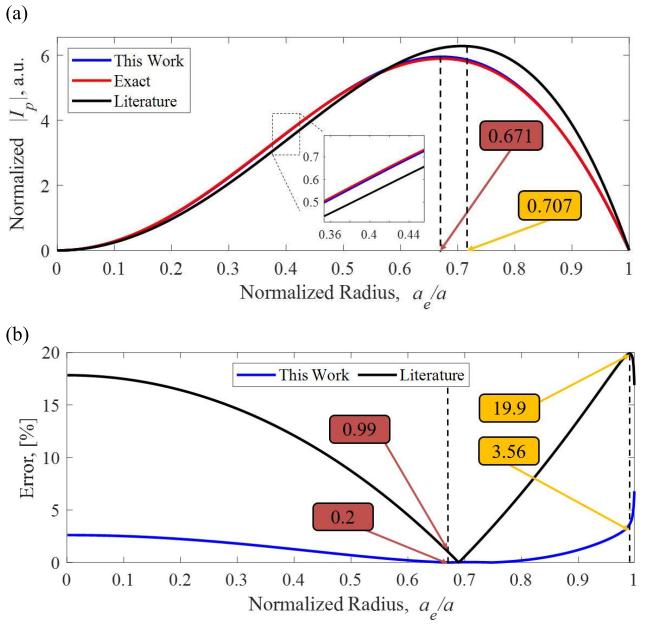

FIGURE 3. **(a) Normalized sum of the strains, I_p with respect to the ratio of the inner electrode radius to the diaphragm radius for the exact solution, literature and this work. (b) Comparison of errors in the literature and this work with respect to the exact solution. The maximum error percentage at the inner electrode and outer electrode regions are indicated in red color and orange color boxes.**

In Fig. 3a, I_p values from the literature and this work are given as a function of the normalized radius that is the ratio of inner electrode radius to the diaphragm radius. In general, ∼60% radius ratio is utilized in literature [20], [37]. However, the true maximum coupling is achieved when the ratio is 67.1%, i.e., the inner electrode radius equals ∼2/3 of the diaphragm radius. Using the mode shape used in literature, the ratio is found as 70.7%. Errors made in the literature and this work with respect to exact solution are given in Fig. 3b. The error made in this work is about 5x smaller than the error made in the literature.

D. ACOUSTIC DOMAIN

In the acoustic domain, a vibrating diaphragm disturbs the medium and creates an acoustic field which can be described by pressure. In this analysis, the vibrating diaphragm is placed in a medium that is considered to be infinitely large such that the boundaries need not to be considered and it is assumed to be homogenous, isotropic, and non-viscous.

The generated pressure field is given by the Rayleigh's integral [24], [28], [32], [42], [43]:

$$p\left(r',\theta',z\right)=\frac{i\rho_m c_m k}{2\pi}\iint_A\left(\frac{\partial w\left(r,\theta,t\right)}{\partial t}\right)\frac{e^{-ikR}}{R}dA \quad (25)$$

where ρ_m is the density of the medium; c_m is the acoustic velocity in the medium; k is the wave number given as ω/c_m; and R is the distance vector between the point N in the

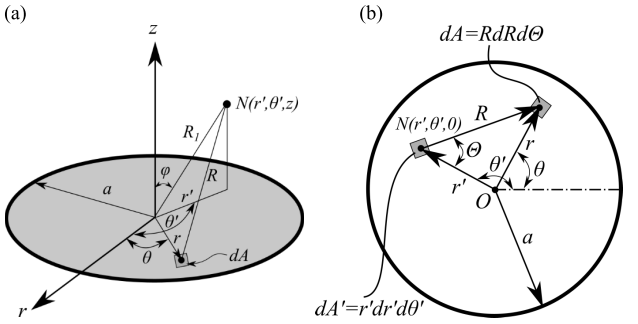

FIGURE 4. **Coordinate system used in the acoustic domain. (a) Point $N(r',\theta',z)$ is defined in the acoustic medium as a point of interest and pressure at point N generated by an infinitesimal area on the surface. (b) Coordinate system used in the calculation of the radiation impedance describing the pressure on an infinitesimal area on the surface generated by another infinitesimal area on the same surface ($z = 0$).**

medium and the differential element on the vibrating surface as shown in Fig. 4a. The acoustic field created by the vibrating surface is divided into two regions: the near and far field. In the near field, energy transfer between the vibrating mass and the surrounding medium takes place in both directions. Hence, the acoustic medium does not travel away from the surface. Although this near field does not affect the far field solution, it is important in the mechano acoustic efficiency of the transducer. The term of wave propagation is defined in the far field, since the wave travels away from the source. The transferred acoustic power is proportional to the radiation resistance of the medium. Therefore, the impedance at the surface which is also called the radiation impedance is important and it is given by the pressure at the surface devided by the surface velocity. The pressure at the surface is given by Rayleigh's integral; however, this time the point of interest, N, is on the surface (Fig. 4b).

The velocity profile is obtained using the displacement profile derived in the mechanical domain analysis, and the differential elements are shown in Fig. 4b. The transformation relation between the cordinates are given as [32]:

$$\begin{aligned} r &= \sqrt{r'^2+R^2-2r'R\cos\left(\Theta\right)} \\ R_{\max} &= r'\cos\left(\Theta\right)+\sqrt{a^2-r'^2\sin^2\left(\Theta\right)} \end{aligned} \quad (26)$$

where R_{max} is the maximum value for a given pair of (r', Θ). The limits of the Rayleigh's integral in the R corrdinate is from 0 to R_{max}. The acoustic impedance is given as the ratio of the force on a point devided by the velocity of the surface [32].

$$\begin{aligned} z_a &= \frac{F_a}{v_a} \\ &= \frac{\iint_A p\left(r,0\right)dA}{v_a} = \frac{\rho_m c_m}{\pi a^2}\left(1-\frac{J_1\left(2ka\right)}{ka}+j\frac{K_1\left(2ka\right)}{ka}\right) \end{aligned} \quad (27)$$

where J_1 and K_1 are the Bessel and Struve functions of first order. These functions are difficult to work with and the

TABLE 2. Comparison values of normalized resistive and reactive radiation impedance components for piston vibrator, this work, exact solution and finite element simulation results.

	r_a				x_a			
ka	Piston Vibrator	This Work	Exact Solution[32]	FEM Results	Piston Vibrator	This Work	Exact Solution[32]	FEM Results
0.1	0.0056	0.0056	0.0050	0.0040	0.0846	0.0930	0.0933	0.0924
0.2	0.0204	0.0204	0.0199	0.0196	0.1678	0.1849	0.1855	0.1837
0.3	0.0446	0.0447	0.0445	0.0443	0.2485	0.2746	0.2753	0.2723
0.4	0.0785	0.0790	0.0785	0.0780	0.3250	0.3606	0.3617	0.3576
0.5	0.1202	0.1214	0.1213	0.1209	0.3967	0.4424	0.4435	0.4386
0.6	0.1698	0.1725	0.1723	0.1723	0.4620	0.5184	0.5200	0.5138
0.7	0.2262	0.2310	0.2308	0.2307	0.5203	0.5881	0.5900	0.5817
0.8	0.2877	0.2956	0.2960	0.2946	0.5713	0.6512	0.6529	0.6424
0.9	0.3541	0.3666	0.3668	0.3634	0.6129	0.7056	0.7080	0.6964
1.0	0.4234	0.4419	0.4424	0.4379	0.6463	0.7522	0.7547	0.7434
1.5	0.7737	0.8514	0.8532	0.8397	0.6796	0.8495	0.8530	0.8339
2.0	1.0326	1.2198	1.2233	1.1960	0.5347	0.7342	0.7281	0.7144
2.5	1.1307	1.4487	1.4538	1.4118	0.3233	0.4782	0.4818	0.4616
3.0	1.0922	1.5041	1.5106	1.4589	0.1596	0.1878	0.1907	0.1826
3.5	1.0013	1.4187	1.4262	1.3739	0.0990	-0.0427	-0.0405	-0.0326
4.0	0.9414	1.2646	1.2758	1.2280	0.1221	-0.1640	-0.1628	-0.1426
4.5	0.9456	1.1163	1.1246	1.0901	0.1663	-0.1811	-0.1805	-0.1562
5.0	0.9913	1.0195	1.0280	0.9990	0.1783	-0.1348	-0.1341	-0.1132

pMUTs works in small *ka* region, in general. The acoustic radiation impedance is simplified as [32]:

$$z_a = R_a + iX_a = \frac{\rho_m c_m}{\pi a^2}(r_a + ix_a) \tag{28}$$

where R_a is the resistive and X_a is the reactive term. Power in the mechanical domain is transferred to the acoustical domain through the resistive term. In addition, r_a and x_a are dimessionless resistive and reactive terms, respectively, and they are more convinient to use for the comparison pusposes. Fig. 5a and 5b show the comparison of results from the literature (a piston vibrator), this work, and Finite Element Simulation (FEM). It is found that there is an approximate frequency after which, both resistance and reactance values are close in all three solutions [44]. In general, ultrasonic transducers work in the low *ka* ($\ll$1) values where k is the wave number and a is the radius in which all solutions converge. Table 2 gives the detailed numerical values for small *ka* for the dimensionless resistive and reactance components of the radiation acoustic impedance in the piston vibrator, exact solution, this work and FEM results.

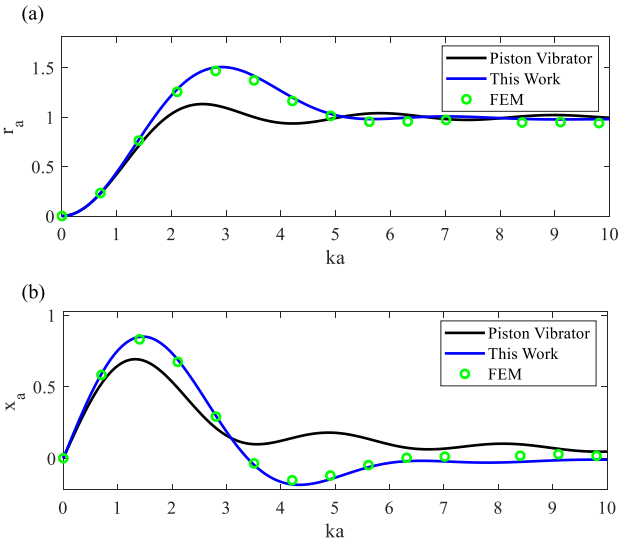

FIGURE 5. Comparison of the dimensionless (a) resistance, r_a, and (b) reactance, x_a, for a piston vibrator, this work, and FEM simulations as a function of wave number multiplied by the radius of the circular diaphragm (*ka*).

E. LUMPED PARAMETERS AND EQUIVALENT CIRCUIT MODEL

Equivalent circuit models are powerful tools when working in multi-physics as in the case of piezoelectric ultrasound transducers [27]. As explained above, there are three energy domains and couplings in the transduction path: electrical, mechanical, and acoustical. Instead of analyzing the structures in three dimensional manners using partial differential equations which can be computationally demanding and physically non-intuitive, they can be analyzed in simplified representations as an electrical equivalent circuit. In addition to being computational friendly, electrical circuit models enable designer to see the energy and power flow not only in the electrical domain but also in all physical domains [45]. In the equivalent circuit analysis, lumped parameters are used as circuit elements in each domain. Most general electro-mechano-acoustical equivalent circuit is given in Fig. 6a for ultrasonic transducers. Each physical domain and corresponding effort and flow variables are given. In the electrical domain, an electrical voltage V_{in} is the effort variable

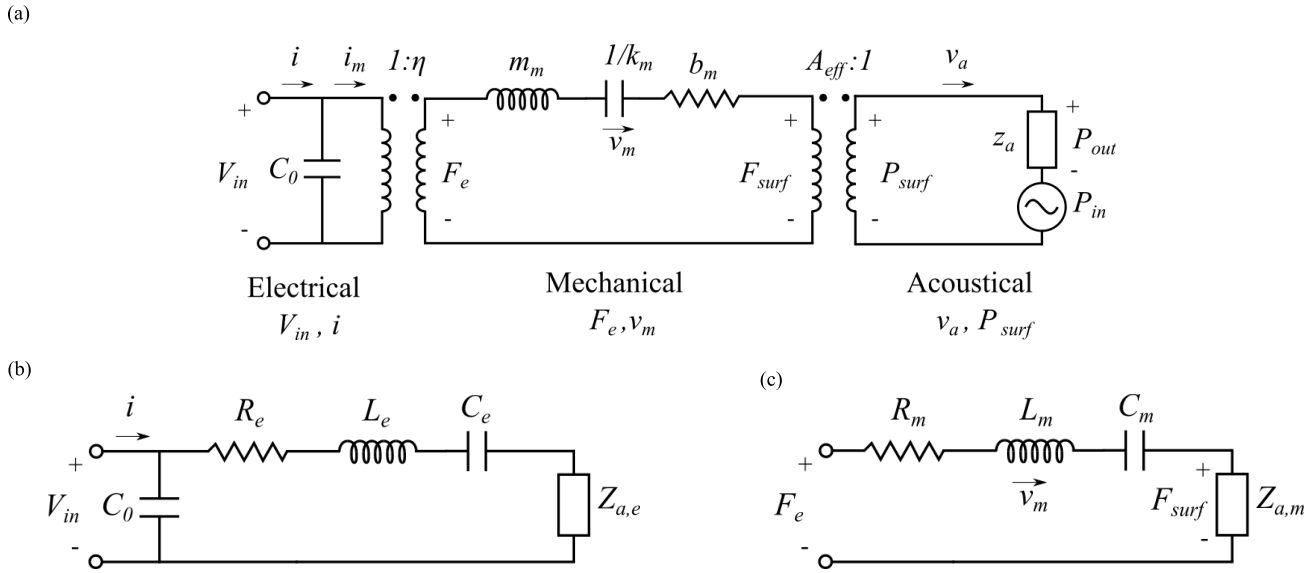

FIGURE 6. (a) Most general form of the equivalent circuit showing all three physical domains separately. Each domain and corresponding effort and flow variables are given with ideal transformers. (b) Butterworth–Van dyke (BVD) representation of the most general equivalent circuit together with acoustic domain impedance shown separately. All the domains are transformed into the electrical domain. (c) Equivalent circuit used in the velocity and displacement calculations. All domains are transformed into the mechanical domain.

and defines the potential difference between electrodes and current, i, which is the flow variable. C_0 is the electrical clamped capacitance also called as feedthrough capacitance obtained from the electrical enthalpy given in equation (22). Electrical and mechanical domains are coupled with an ideal transformer having the turns ratio of η. It is defined by the coupling enthalpy given in equation (23), that is:

$$H_{Coupling} = \eta V_e w(0) = -e_{31,f} V_e Z_p I_P$$
$$\eta = -e_{31,f} Z_p I_P \tag{29}$$

The transformer turns ratio is defined as the ratio of effort variables in the coupled domains:

$$\eta = \frac{F_e}{V_{in}} \tag{30}$$

In the mechanical domain, the generated piezoelectric force F_e is the effort variable and the velocity of the vibrating mass v_m is the flow variable. The symbols m_m, k_m, and b_m are equivalent mechanical mass, stiffness and damping, respectively. Similarly, mechanical and acoustical domains are coupled with another ideal transformer having the turns ratio of A_{eff}. This is also a well-known relation between the force and pressure.

$$A_{eff} = \frac{F_{surf}}{P_{surf}} \tag{31}$$

In the acoustical domain, the surface pressure, P_{surf} is the effort variable and the volumetric velocity, v_a is the flow variable. The total pressure at the surface equals the summation of the output pressure of the transducer P_{out} and the incident pressure in the medium P_{in}. The variable, z_a, represents the acoustic radiation impedance of the vibrating surface in a medium. In the transmitter mode, the incident pressure, P_{in}, is set to be zero. Hence, the output pressure P_{out} equals the surface pressure P_{surf}. Table 3 gives the comparison of each lumped parameters for the exact solution, literature and this work.

III. RESULTS AND DISCUSSIONS

In order to compare the results, the reduced electrical equivalent circuit, also known as Butterworth–Van dyke (BVD) representation, of the pMUT is given Fig. 6b. The terms, R_e, L_e, and C_e represent the electrical resistance, inductance, and capacitance, respectively and $Z_{a,e}$ represents the acoustical impedance transformed into the electrical domain.

The equivalent circuit used in the surface average velocity and displacement calculations is given Fig. 6c, where R_m, L_m, and C_m are the mechanical resistance, inductance, and capacitance, respectively and $Z_{a,m}$ represents the acoustical impedance transformed into the mechanical domain. All of these transformed electrical and mechanical domain parameters are given in Table 4.

The results of the equivalent circuits for this work, exact solution, and literature are examined and compared with FEM simulations. In all results, the specific and simplest case of pMUT is the single electrode and unimorph structure in the air medium. The piezoelectric material is selected to be AlN which is one of the most commonly used piezoelectric material [50]. In order to ease the complexities, the elastic layer is also selected to be AlN. All material properties, dimensions and medium properties are given in Table 5.

TABLE 3. Comparison equivalent circuit parameters obtained from exact solution, for piston vibrator, and this work.

Parameter	Exact Solution	Literature	This Work
Clamped capacitance*, C_0	$0.449\frac{\varepsilon^{S}{}_{33}\pi a^2}{h_p}\left(1-k_{31}{}^2\right)$	$0.49\frac{\varepsilon^{S}{}_{33}\pi a^2}{h_p}\left(1-k_{31}{}^2\right)$	$0.449\frac{\varepsilon^{S}{}_{33}\pi a^2}{h_p}\left(1-k_{31}{}^2\right)$
Turns Ratio, η	$2\pi(0.938)e_{31,f}Z_p$	$2\pi e_{31,f}Z_p$	$2\pi(0.947)e_{31,f}Z_p$
Mass, m_m	$0.183\pi a^2\Lambda$	$0.2\pi a^2\Lambda$	$0.184\pi a^2\Lambda$
Stiffness, k_m	$19.073\pi\frac{D}{a^2}$	$21.333\pi\frac{D}{a^2}$	$19.226\pi\frac{D}{a^2}$
Damping**, b_m	Neglected	Neglected	Neglected
Effective Surface Area, A_{eff}	$0.312A_{tot}$	$\frac{1}{3}A_{tot}$	$0.313A_{tot}$
Acoustic radius***, a_c	$0.558a$	$\frac{1}{\sqrt{3}}a$	$0.559a$
Radiation Impedance****, z_a	$\frac{\rho_m c_m}{A_{eff}}\left(r_a+ix_a\right)$	$\frac{\rho_m c_m}{A_{eff}}\left(r_a+ix_a\right)$	$\frac{\rho_m c_m}{A_{eff}}\left(r_a+ix_a\right)$

* : Electrode coverage ratio is taken as 0.67, 0.7, and 0.67 for exact, literature, and this work, respectively.
** : Mechanical damping is small, assumption: $\mathrm{Re}(Z_a)>>b_m$, [46]
*** : The given mode shapes in TABLE I are normalized such that the maximum displacement over the surface are is unity.
**** : The values of r_a and x_a can be obtained either integration of the given integral in equation (27) or as given in TABLE II for respective solution.

TABLE 4. Equivalent circuit parameter transformed into electrical and mechanical domains.

Electrical Domain, [Unit]	Mechanical Domain, [Unit]
$L_e=\frac{m_m}{\eta^2}$, $[H]$	$L_m=m_m$, $[kg]$
$C_e=\frac{\eta^2}{k_m}$, $[F]$	$C_m=\frac{1}{k_m}$, $[m/N]$
$R_e=\frac{b_m}{\eta^2}$, $[\Omega]$	$R_m=b_m$, $[kg/s]$
$Z_{a,e}=\frac{A_{eff}{}^2 z_a}{\eta^2}$, $[\Omega]$	$Z_{a,m}=A_{eff}{}^2 z_a$, $[kg/s]$

TABLE 5. Summary of the dimensions and material properties for comparison study.

Parameter	Value
AlN Modulus of elasticity [47], Y	348 GPa
AlN Poisson's Ratio [47], v	0.3
AlN Density [4, 5, 47], ρ	3300 kg/m^3
AlN Dielectric constant [47], ε_r	10.26
Piezoelectric coefficient [4, 5, 48], $e_{31,eff}$	-1.02 C/m^2
Layer thickness, h_1 and h_2	1 µm
Radius, a	200 µm
Air density [49], ρ_m	1.23 kg/m^3
Speed of sound in air [49], c_m	343 m/s

Frequency response, on-axis pressure at small and large ka values, single element input impedance, bandwidth, quality factor, and directivity of a single pMUT cell are compared. First, the equivalent input impedance is obtained from the equivalent circuit given in Fig. 6b as follow:

$$Z_{in}=\frac{V_{in}}{i}=\left[sC_0+\frac{\eta^2 s}{s^2m_m+sA_{eff}^2z_a+k_m}\right]^{-1} \tag{32}$$

where s is the frequency parameter equals to $j\omega$. The input impedance comparison is shown in Fig. 7. There is a constant error of 24% in the literature in contrast to an error of 0.005% in this work with respect to the exact solution.

The velocity and displacement of the diaphragm are obtained using the equivalent circuits given in Fig. 6c. The velocity and displacements are given as:

$$\begin{aligned} v_m &= \frac{F_e}{Z_{mechanical}}=\frac{\eta V_{in}s}{s^2m_m+sA_{eff}{}^2z_a+k_m} \\ u_m &= \frac{\partial w_m}{\partial t}=j\omega w_m \end{aligned} \tag{33}$$

Figs. 8a and 8b show the velocity and displacement outputs versus the frequency, respectively, between this work, the literature, exact solution, and FEM. As explain in the mechanical domain analysis, the error made in the literature for the natural frequency calculation has about 1.14% in error and: this error is dropped to 0.03% in this work with respect to the exact solution. While both errors are small and good enough to be used in engineering purposes, this work provides much

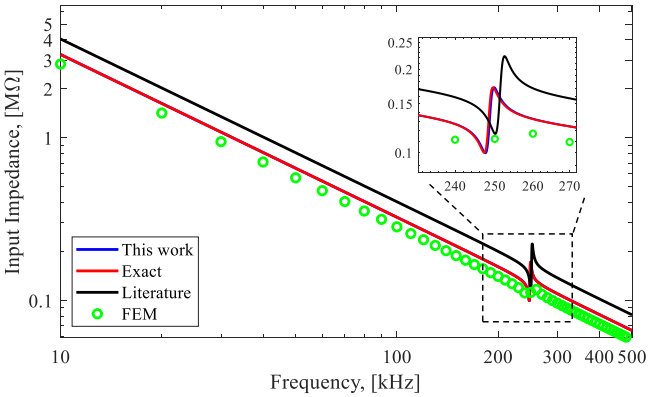

FIGURE 7. Electrical input impedance comparison for this work, exact solution, literature, and FEM. Zoomed-in image shows the region around the resonance of the diaphragm.

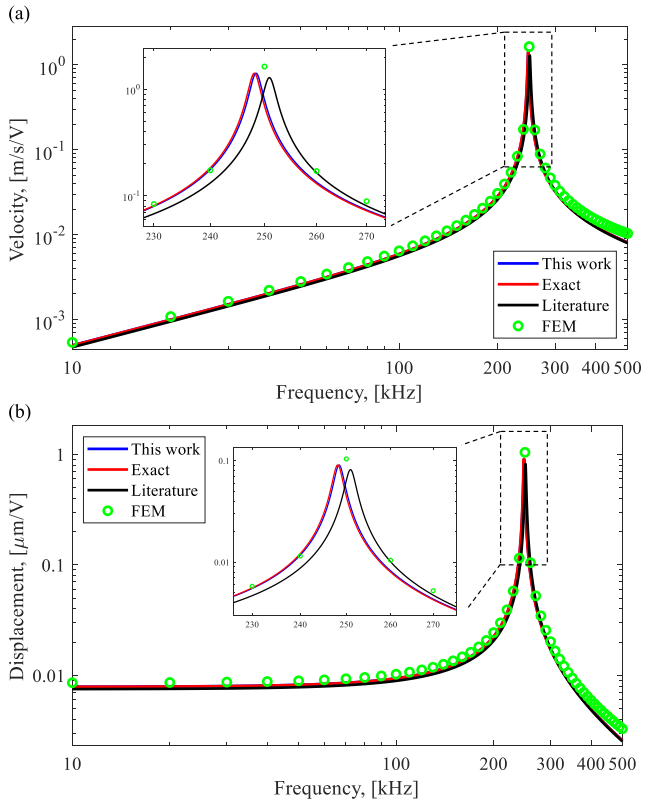

FIGURE 8. (a) Velocity and (b) and displacement comparisons for this work, exact solution, and literature. The zoomed-in images show the regions around the mechanical resonance.

better accuracy for the natural frequency. The overall velocity error in the literature is around 4.7% and it drops to 0.16% in this work.

In this study, it is assumed that the dominating damping (B_m) is coming from the acoustic radiation impedance on the surface due to the air medium. Hence, mechanical damping factors including thermomechanical damping, anchor loss, etc. are neglected (b_m=0) and the damping factor is simplified as:

$$B_m = 2\mathrm{Re}(Z_{a,m}) = 2\rho_m c_m \pi {a_c}^2 r_a \tag{34}$$

where the multiplier 2 comes from the fact that medium is on both sides of the diaphragm. The transducer bandwidth (BW) and quality factor (Q) are given as:

$$BW = \frac{1}{2\pi}\frac{B_m}{m_m} = \frac{1}{\pi}\frac{\rho_m c_m \pi {a_c}^2 r_a}{m_m}$$
$$Q = \frac{\sqrt{m_m k_m}}{B_m} = \frac{\sqrt{m_m k_m}}{2\rho_m c_m \pi {a_c}^2 r_a} \tag{35}$$

Bandwidth and quality factor comparisons between this work, the literature, and exact solution are given in Figs. 9a and 9b, respectively. The bandwidth, BW, error in the literature with respect to the exact solution drops from 4.9% to a value of 0.17% in this work. Similarly, the quality factor error drops from 3.5% to 0.04%.

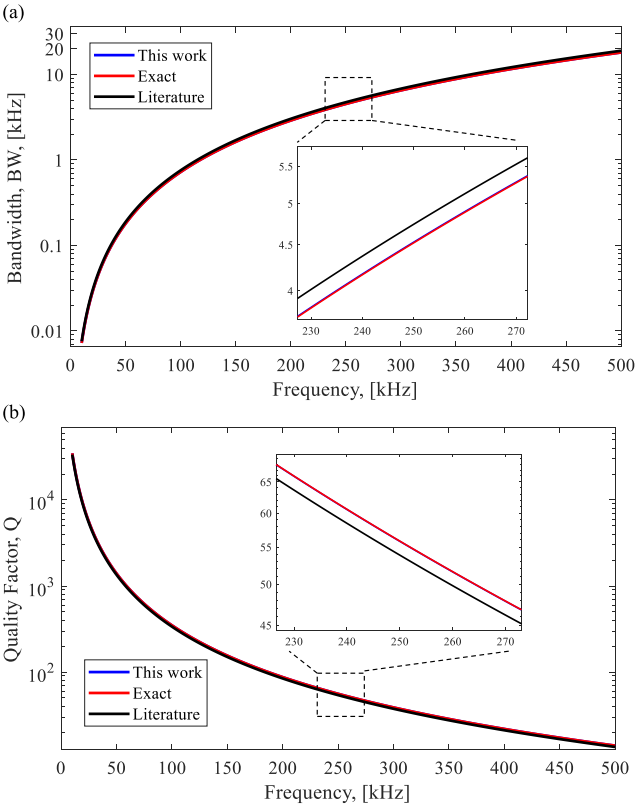

FIGURE 9. (a) Bandwidth, and (b) quality factor comparisons for this work, the exact solution, and literature. The zoomed-in images show the regions around the mechanical resonance. Results of this work and the exact solution are very close such that the blue color line (this work) is not visible in the figure.

The directionality is defined as the ratio of the far field pressure at a specific angle, φ as shown in Fig. 4a to the on axis pressure at $\varphi = 0°$. Using the pressure equation given in

equation (25), the directionality, D(φ), is derived as;

$$D(\phi) = \frac{\iint\limits_A \left(\frac{\partial w(r,\theta,t)}{\partial t}\right) \frac{e^{-ikR}}{R} dA}{\iint\limits_A \left(\frac{\partial w(r,\theta,t)}{\partial t}\right) dA} \tag{36}$$

where the vector distance between the infinitesimal element on the surface and the point in medium, R, is:

$$\begin{aligned} R^2 &= R_1^2 - r^2 - 2R_1 r \sin(\varphi)\cos(\theta) \\ R &\approx R_1 - r\sin(\varphi)\cos(\theta), \quad R_1 \gg a \end{aligned} \tag{37}$$

Fig. 10 shows the result of the directionality for different *ka* values, i.e., frequencies. For the very low $ka \ll 1$ values, all the approaches have good approximation for the directionality. As the *ka* values increases, the error between the literature and the exact solution increases, while results in this work follows the exact solution more closely. It is noted that the piston vibrator approximation is used in literature whereas the two-term mode shape is used in this study.

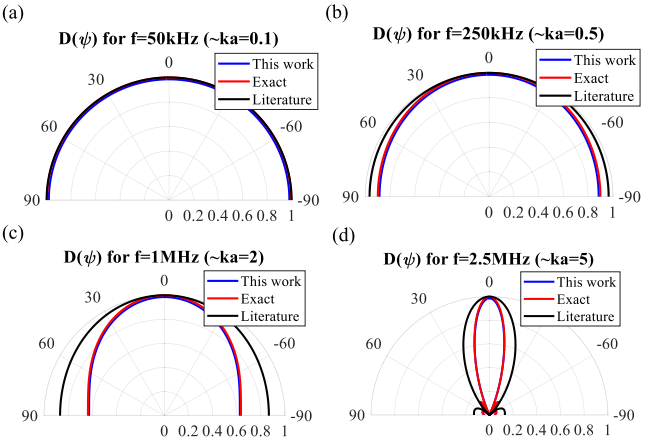

FIGURE 10. (a-d) The directivity comparison for this work, the exact solution, and literature. The directivity is shown for different frequencies, i.e., *ka* values.

Lastly, the on-axis pressure is calculated by setting $\varphi = 0°$ in the pressure calculation equation and the Rayleigh's integral and the sectorial distance, R, become [24], [28], [32], [42], [43]:

$$p(r', \theta', z) = \frac{i\rho_m c_m k}{2\pi} \iint\limits_A \left(\frac{\partial w(r,\theta,t)}{\partial t}\right) \frac{e^{-ikR}}{R} dA$$

$$R = \sqrt{R_1^2 + r^2} \tag{38}$$

Fig. 11a shows the on-axis pressure as a distance from the surface is given for the resonance frequency. In this region, i.e., small *ka* values, all the approaches capture similar behavior for the near and far field pressure. Fig. 11c shows the error of the on-axis pressure from the literature is around 15% in the near field and 7% in the far field. In this work, these errors drop to 0.34% and 0.38% in the near field and far field, respectively. Similarly, Fig. 11b shows the on-axis pressure at

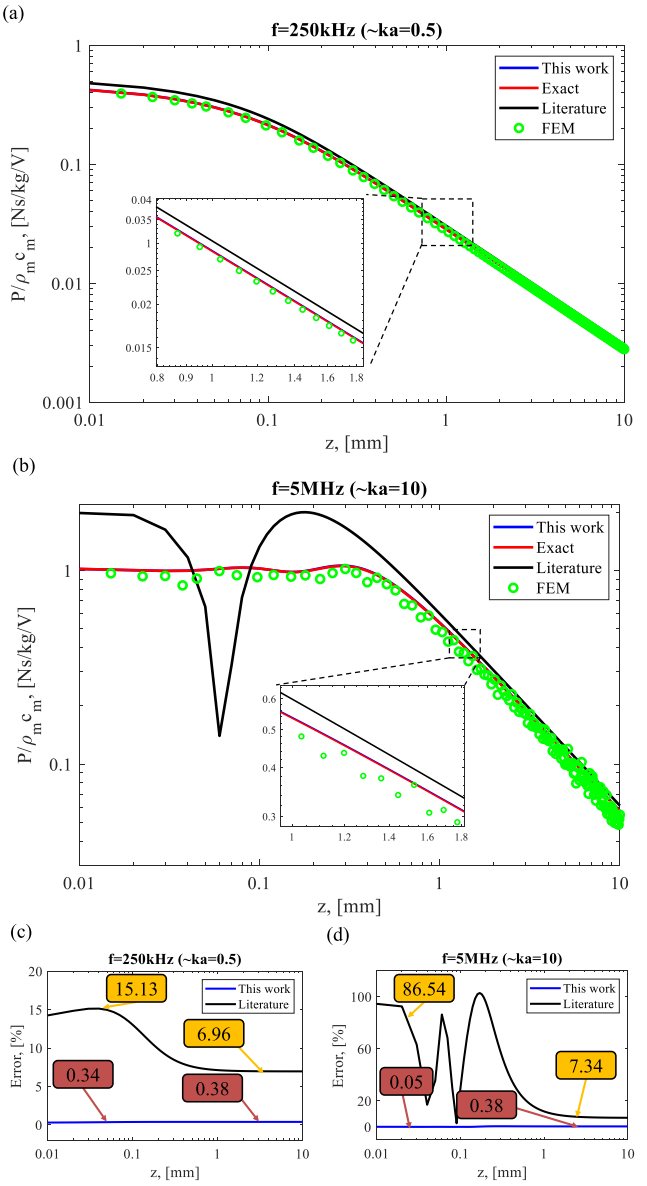

FIGURE 11. On-axis pressure at a distance *z* from the diaphragm surface at: (a) 250 kHz corresponding to a small ka value ~0.5; and (b) 5 MHz corresponding to a large *ka* value ~10. The error of the on-axis pressure for: (c) 250 kHz and (d) 5 MHz of vibration frequency of the diaphragm. The near and far fields errors are separately indicated in both frequencies.

high *ka* values. In the near field, the literature results have the error of more than 80 and this work has only 0.05% error as shown in Fig. 11d. All the approaches capture the far field on-axis pressure behavior for high *ka* values and the error in the literature is around 7% and it decreases to 0.38% in this work.

IV. CONCLUSION

An improved, two-term mode shape approximation for the circular-shape pMUT has been demonstrated. The small signal electro-mechano-acoustic equivalent model can analyze

many parameters such as individual equivalent circuit parameters, input impedance, frequency, bandwidth, quality factor, directivity, and the on-axis pressure in the near and far fields. The proposed model was compared with the literature, exact solution and finite element method simulations. The error in all these parameters are decreased below 0.5% compared to exact solution. In addition, enhancements in these parameters compared to literature error ranges from 5x to three orders of magnitude. We found that the correct modelling of deformation shape is critical for the model accuracy. The approximate energy based method can be utilized to obtain more accurate mode shapes and parameters for different types of ultrasonic transducers such as rectangle, ring geometries and dual electrode, bimorph structures.

REFERENCES

[1] I. O. Wygant *et al.*, "Integration of 2D CMUT arrays with front-end electronics for, volumetric ultrasound imaging," *IEEE Trans. Ultrason., Ferroelectr., Frequency Control*, vol. 55, no. 2, pp. 327–342, Feb. 2008.

[2] X. Jin, I. Ladabaum, F. Degertekin, S. Calmes, and B. T. Khuri-Yakub, "Fabrication and characterization of surface micromachined capacitive ultrasonic immersion transducers," *J. Microelectromech. Syst.*, vol. 8, no. 1, pp. 100–114, Mar. 1999.

[3] Z. Shao, S. Pala, Y. Peng, and L. Lin, "Bimorph pinned piezoelectric micromachined ultrasonic transducers for space imaging applications," *J. Microelectromech. Syst.*, vol. 30, no. 4, pp. 650–658, Aug. 2021.

[4] R. J. Przybyla, H. Y. Tang, A. Guedes, S. E. Shelton, D. A. Horsley, and B. E. Boser, "3D ultrasonic rangefinder on a chip," *IEEE J. Solid-State Circuits*, vol. 50, no. 1, pp. 320–334, Jan. 2015.

[5] R. Przybyla, "Ultrasonic 3D rangefinder on a chip," Doctor Philosophy, Elect. Eng. Comput. Sci., Univ. California Berkeley, Berkeley, CA, USA, Tech. Rep. UCB/EECS-2016-4, 2013.

[6] H.-Y. Tang *et al.*, "3-D ultrasonic fingerprint sensor-on-a-chip," *IEEE J. Solid-State Circuits*, vol. 51, no. 11, pp. 2522–2533, Nov. 2016.

[7] Y. Lu *et al.*, "Ultrasonic fingerprint sensor using a piezoelectric micromachined ultrasonic transducer array integrated with complementary metal oxide semiconductor electronics," *Appl. Phys. Lett.*, vol. 106, no. 26, Jun. 2015, Art. no. 263503.

[8] S. Pala, Z. Shao, Y. Peng, and L. Lin, "Ultrasond-induced haptic sensations via PMUTS," in *Proc. IEEE 34th Int. Conf. Micro Electro Mech. Syst. (MEMS)*, Jan. 2021, pp. 911–914.

[9] T. Hoshi and H. Shinoda, "Airborne ultrasound tactile display," in *Pervasive Haptics: Science, Design, and Application*, H. Kajimoto, S. Saga, and M. Konyo, Eds. Tokyo, Japan: Springer, 2016, pp. 121–138.

[10] R. J. Przybyla, H.-Y. Tang, S. E. Shelton, D. A. Horsley, and B. E. Boser, "12.1 3D ultrasonic gesture recognition," in *IEEE Int. Solid-State Circuits Conf. (ISSCC) Dig. Tech. Papers*, Feb. 2014, pp. 210–211.

[11] Z. Shao, S. Pala, Y. Liang, T. Jiang, and L. Lin, "Non-contact surface temperature sensing based on a single bimorph pMUTs array," in *Proc. IEEE 33rd Int. Conf. Micro Electro Mech. Syst. (MEMS)*, Jan. 2020, pp. 861–864.

[12] S. Pala, Y. Liang, B. Eovino, Z. Shao, and L. Lin, "Radius of curvature measurement using piezoelectric micromachined ultrasonic transducers," in *Proc. IEEE 33rd Int. Conf. Micro Electro Mech. Syst. (MEMS)*, Jan. 2020, pp. 865–868.

[13] F. Y. Yamaner, S. Olcum, H. K. Oguz, A. Bozkurt, H. Koymen, and A. Atalar, "High-power CMUTs: Design and experimental verification," *IEEE Trans. Ultrason., Ferroelectr., Freq. Control*, vol. 59, no. 6, pp. 1276–1284, Jun. 2012.

[14] S. Tadigadapa and K. Mateti, "Piezoelectric MEMS sensors: State-of-the-art and perspectives," *Meas. Sci. Technol.*, vol. 20, no. 9, Sep. 2009, Art. no. 092001.

[15] O. Oralkan *et al.*, "Experimental characterization of collapse-mode CMUT operation," *IEEE Trans. Ultrason., Ferroelectr., Freq. Control*, vol. 53, no. 8, pp. 1513–1523, Aug. 2006.

[16] F. Sammoura, S. Akhbari, and L. Lin, "An analytical solution for curved piezoelectric micromachined ultrasonic transducers with spherically shaped diaphragms," *IEEE Trans. Ultrason., Ferroelectr., Freq. Control*, vol. 61, no. 9, pp. 1533–1544, Sep. 2014.

[17] B. E. Eovino, S. Akhbari, and L. Lin, "Broadband ring-shaped PMUTS based on an acoustically induced resonance," in *Proc. IEEE 30th Int. Conf. Micro Electro Mech. Syst. (MEMS)*, Las Vegas, NV, USA, Jan. 2017, pp. 1184–1187.

[18] S. Pala and L. Lin, "Piezoelectric micromachined ultrasonic transducers (pMUT) with free boundary," in *Proc. IEEE Int. Ultrason. Symp. (IUS)*, Sep. 2020, pp. 1–4.

[19] Y. Liang, B. Eovino, and L. Lin, "Piezoelectric micromachined ultrasonic transducers with pinned boundary structure," *J. Microelectromech. Syst.*, vol. 29, no. 4, pp. 585–591, Aug. 2020.

[20] S. Akhbari, F. Sammoura, B. Eovino, C. Yang, and L. Lin, "Bimorph piezoelectric micromachined ultrasonic transducers," *J. Microelectromech. Syst.*, vol. 25, no. 2, pp. 326–336, Apr. 2016.

[21] P. Muralt *et al.*, "Piezoelectric micromachined ultrasonic transducers based on PZT thin films," *IEEE Trans. Ultrason., Ferroelectr., Freq. Control*, vol. 52, no. 12, pp. 2276–2288, Dec. 2005.

[22] S. Trolier-McKinstry and P. Muralt, "Thin film piezoelectrics for MEMS," *J. Electroceramics*, vol. 12, nos. 1–2, pp. 7–17, Jan. 2004.

[23] R. Hamming, *Numerical Methods for Scientists and Engineers*. New York, NY, USA: Dover, 1987.

[24] L. L. Beranek and T. Mellow, *Acoustics: Sound Fields and Transducers*. Oxford, U.K.: Academic is an Imprint of Elsevier, 2012.

[25] H. Koymen *et al.*, "An improved lumped element nonlinear circuit model for a circular CMUT cell," *IEEE Trans. Ultrason., Ferroelectr., Freq. Control*, vol. 59, no. 8, pp. 1791–1799, Aug. 2012.

[26] K. Smyth and S. G. Kim, "Experiment and simulation validated analytical equivalent circuit model for piezoelectric micromachined ultrasonic transducers," *IEEE Trans. Ultrason., Ferroelectr., Freq. Control*, vol. 62, no. 4, pp. 744–764, Apr. 2015.

[27] W. P. Mason, *Electromechanical Transducers Wave Filters*. New York, NY, USA: D.Van Nostrand, 1948.

[28] L. Rayleigh, *The Theory of Sound*, 2nd ed. New York, NY, USA: Dover, 1894.

[29] S. Timoshenko, *Vibration Problems in Engineering*, 2nd ed. New York, NY, USA: D. Van Nostrand Company, 1937.

[30] P. M. Morse and K. U. Ingard, *Theoretical Acoustics*. San Francisco, CA, USA: McGraw-Hill, 1968.

[31] A. W. Leissa, *Vibrations of Plates*. Washington, DC, USA: Office of Technology Utilization National Aeronautics and Space Administration, 1969.

[32] D. T. Blackstock, *Fundamentals of Physical Acoustics*. Hoboken, NJ, USA: Wiley, 2000.

[33] S. S. Rao, *Vibration of Continuous Systems*. Hoboken, NJ, USA: Wiley, 2007.

[34] S. Timoshenko and S. Woinowsky-Krieger, *Theory of Plates and Shells*. San Francisco, CA, USA: McGraw-Hill, 1987.

[35] S. S. Rao, *Mechanical Vibrations*, 5th ed. Upper Saddle River, NJ, USA: Prentice-Hall, 2011.

[36] S. Pala and K. Azgın, "A MEMS square Chladni plate resonator," *J. Micromech. Microeng.*, vol. 26, no. 10, Oct. 2016, Art. no. 105016.

[37] Y. Lu, Q. Wang, and D. A. Horsley, "Piezoelectric micromachined ultrasonic transducers with increased coupling coefficient via series transduction," in *Proc. IEEE Int. Ultrason. Symp. (IUS)*, Oct. 2015, pp. 1–4.

[38] R. D. Mindlin, "High frequency vibrations of piezoelectric crystal plates," *Int. J. Solids Struct.*, vol. 8, pp. 895–906, Jul. 1972.

[39] H. F. Tiersten, "Hamilton's principle for linear piezoelectric media," *Proc. IEEE*, vol. 55, no. 8, pp. 1523–1524, Aug. 1967.

[40] W. P. Mason, *Piezoelectric Crystals and Their Applications to Ultrasonics*. New York, NY, USA: Can Nostrand 1950.

[41] M. H. Sadd, *Elasticity: Theory, Applications, and Numerics*, 2nd ed. Oxford, U.K.: Academic, 2009.

[42] J. L. Butler and C. H. Sherman, *Transducers and Arrays for Underwater Sound*. Cham, Switzerland: Springer, 2016.

[43] G. S. Kino, *Acoustic Waves: Devices, Imaging, and Analog Signal Processing*. Englewood Cliffs, NJ, USA: Prentice-Hall, 1987.

[44] R. L. Pritchard, "Mutual acoustic impedance between radiators in an infinite rigid plane," *J. Acoust. Soc. Amer.*, vol. 32, no. 6, pp. 730–737, Feb. 1960.

[45] S. D. Senturia, *Microsystem Design*. Boston, MA, USA: Kluwer, 2001.

[46] D. A. Horsley *et al.*, "Piezoelectric micromachined ultrasonic transducers for human-machine interfaces and biometric sensing," in *Proc. IEEE Sensors*, Nov. 2015, pp. 1507–1510.

[47] S. Akhbari, F. Sammoura, and L. Lin, "Equivalent circuit models for large arrays of curved and flat piezoelectric micromachined ultrasonic transducers," *IEEE Trans. Ultrason., Ferroelectr., Freq. Control*, vol. 63, no. 3, pp. 432–447, Mar. 2016.
[48] M.-A. Dubois and P. Muralt, "Properties of aluminum nitride thin films for piezoelectric transducers and microwave filter applications," *Appl. Phys. Lett.*, vol. 74, no. 20, pp. 3032–3034, 1999.
[49] O. Cramer, "The variation of the specific heat ratio and the speed of sound in air with temperature, pressure, humidity, and CO_2 concentration," *J. Acoust. Soc. Amer.*, vol. 93, no. 5, pp. 2510–2516, May 1993.
[50] S. Akhbari, A. Voie, Z. Li, B. Eovino, and L. Lin, "Dual-electrode bimorph pMUT arrays for handheld therapeutic medical devices," in *Proc. IEEE 29th Int. Conf. Micro Electro Mech. Syst. (MEMS)*, Jan. 2016, pp. 1102–1105.

SEDAT PALA received the B.S. degree (Hons.) in mechanical engineering, the minor degree in business administration, and the M.S. degree (Hons.) in mechanical engineering from Middle East Technical University (METU), Ankara, Turkey, in 2015, 2015, and 2017, respectively. He is currently pursuing the Ph.D. degree in mechanical engineering with the University of California at Berkeley, Berkeley, CA, USA. He joined METU MEMS Characterization Laboratory in 2014 and has been a Research Assistant for three years. He joined Berkeley Sensors and Actuator Center (BSAC) in 2017. His research interests include design, fabrication, and characterization of MEMS devices, ultrasonic piezoelectric transducers, piezoelectric materials, capacitive transducers, and resonators. He had the graduate scholarship from the Scientific and Technological Research Council of Turkey (TUBITAK) with the code BİDEB 2210 during his M.S. studies.

LIWEI LIN (Member, IEEE) received the B.S. degree in power mechanical engineering from the National Tsing Hua University, Taiwan, in 1986, and the M.S. and Ph.D. degrees in mechanical engineering from the University of California at Berkeley (UC Berkeley) in 1991 and 1993, respectively. After graduation, he was a Senior Research Scientist with BEI Electronics, Inc. He served as an Associate Professor with the National Taiwan University and an Assistant Professor with the University of Michigan, before joining as a Faculty Member with UC Berkeley in 1999. From 2006 to 2009, he was the Vice Chair of graduate study with the Mechanical Engineering Department. He currently serves as the James Marshall Wells Academic Chair with the Department of Mechanical Engineering, UC Berkeley, and the Co-Director of the Berkeley Sensor and Actuator Center (BSAC). He holds 21 patents in MEMS and has authored or coauthored over 290 journal publications. His research interests include MEMS, NEMS, nanotechnology, design and manufacturing of micro sensors and micro actuators, development of micromachining processes by silicon surface/bulk micromachining, micro molding process, and mechanical issues in MEMS, such as heat transfer, solid/fluid mechanics, and dynamics, at UC Berkeley.